

1 SUBMISSION TO:

2 Transport in Porous Media

3 *Special Issue: Uncertainty Quantification and Multiscale Methods for Porous Media*

4

5 DATE:

6 30 July 2017

7

8 TITLE:

9 **Probabilistic study of rainfall-triggered instabilities in randomly heterogeneous**
10 **unsaturated finite slopes**

11

12 AUTHORS:

13 Thi Minh Hue Le¹, Marcelo Sanchez², Domenico Gallipoli³, Simon Wheeler⁴

14

15 AFFILIATIONS:

16 ¹ Norwegian Geotechnical Institute. Sognveien 72, Oslo, Norway; Tel: +47 (0) 9300
17 1834; Email: thi.le@ngi.no

18 ² Zachry Department of Civil Engineering, Texas A&M University, 3136 TAMU,
19 College Station, TX 77843-3136, United States; Tel. (+1) -979- 862 6604; Fax: (+1) -
20 979- 862 7696; Email: msanchez@civil.tamu.edu

21 ³ Laboratoire SIAME, Fédération IPRA, Université de Pau et des Pays de l'Adour, Allée
22 du Parc Montaury, Anglet, 64600, France; Tel : +33 (0)559574280; Email:
23 domenico.gallipoli@univ-pau.fr

24 ⁴ Infrastructure & Environment Research Division, School of Engineering, University of
25 Glasgow, G12 8LT, Glasgow, United Kingdom; Tel: +44 (0)141 330 5201; Fax: +44
26 (0)141 330 4557; Email: Simon.Wheeler@glasgow.ac.uk

27

28

29
30
31
32
33
34
35
36
37
38
39
40
41
42
43
44
45
46

Table of contents

1	Introduction	5
2	Method	8
	2.1 Model geometry	8
	2.2 Hydraulic and mechanical models	10
	2.3 Boundary conditions and simulation process	14
3	Random porosity field	17
4	Influence of hydraulic characteristics	20
	4.1 Water table depth.....	20
	4.2 Saturated permeability	24
	4.3 Rainfall intensity.....	27
	4.4 Soil water retention curve – Parameter η	29
	4.5 Soil water retention curve – Parameter m	32
5	Conclusions	36
6	Acknowledgements	37
7	References	37

47 **Abstract**

48

49 Water infiltration destabilises unsaturated soil slopes by reducing matric suction, which
50 produces a decrease of material cohesion. If the porosity of the soil is spatially
51 heterogeneous, a degree of uncertainty is added to the problem as water tends to follow
52 preferential paths and produces an irregular spatial distribution of suction. This study
53 employs the finite element method together with Monte Carlo simulations to quantify the
54 effect of random porosity on the uncertainty of both the factor of safety and failure size of
55 an unsaturated finite slope during and after a rainfall event. The random porosity is
56 modelled using a univariate random field. Results show that, under partially saturated
57 conditions, the random heterogeneity leads to a complex statistical variation of both
58 factor of safety and failure size during the rainfall event. At any given time, the
59 uncertainty about failure size is directly linked to the uncertainty about the position of the
60 wetting front generated by infiltration. Interestingly, the statistical mean of the failed area
61 is smallest when the mean of the factor of safety is lowest. In other words, the slope
62 becomes more likely to fail but the size of the failure mass tends to be limited.

63 The study also investigates the sensitivity of failure uncertainty to external hydraulic
64 parameters (i.e. initial water table depth, rainfall intensity) and internal soil parameters
65 (i.e. permeability and water retention characteristics). In general, the sensitivity increases
66 when the effect of these parameters on the spatial variation of suction is stronger.

67

68

69

70 **1 Introduction**

71 Catastrophic failures of soil slopes caused by rainfall infiltration are relatively common
72 but their triggering mechanisms are still poorly understood. This is particularly true in
73 unsaturated slopes where the spatial variability of suction and degree of saturation
74 induces an uneven distribution of permeability inside the soil mass. This also means that,
75 unlike in saturated soils, the permeability of unsaturated soils does not remain constant
76 during the rainfall. The high non-linearity of the constitutive equations linking the soil
77 suction (or saturation) to permeability and the coupling between soil porosity and degree
78 of saturation make the numerical solution of these problems very challenging.

79

80 Further complexities are introduced by the heterogeneity of porosity, which influences
81 the infiltration pattern and hence the stability of the slope. In a heterogeneous slope,
82 water will preferably infiltrate through paths connecting high permeability areas, which
83 in turn produces a spatially irregular distribution of suction and saturation inside the soil
84 mass (Le et al. 2012). Soil elements experiencing an earlier loss of suction will also
85 undergo an earlier reduction of strength compared to other elements where suction
86 changes are slower. At any given time, the likely slip surface will therefore tend to pass
87 through these weaker elements, which may result in a lower safety factor compared to a
88 homogenous slope.

89

90 A relatively large number of probabilistic studies have investigated the effect of material
91 uncertainties on the safety of dry or saturated slopes. Many of them have employed the
92 finite element method (FEM), which is particularly suited to the description of spatial
93 heterogeneity, to analyse the effect of strength variability on slope safety (Hicks 2005;
94 Griffiths and Fenton 2004). Other studies have instead employed the limit equilibrium
95 method (LEM) because of its simplicity (Pathak et al. 2007; El-Ramly et al. 2005).
96 Stochastic studies of slope instabilities in randomly heterogeneous slopes have relied on
97 Monte Carlo simulations to handle complicated geometries and variability patterns
98 without requiring over-simplified assumptions. Results from these simulations, and from

99 practical observations, have repeatedly indicated that material heterogeneity affects
100 strongly the stability of soil slopes (Alonso 1976; Babu and Mukesh 2004; El-Ramly et
101 al. 2005; Griffiths and Fenton 2004; Griffiths and Marquez 2007; Hicks and Onisiphorou
102 2005; Hicks and Samy 2002; Hicks and Spencer 2010; Mostyn and Li 1993; Mostyn and
103 Soo 1992; Sejnoha et al. 2007; Cho 2009; Fenton and Griffiths 2005; Griffiths et al.
104 2015). The majority of stochastic studies adopted the Monte Carlo approach because of
105 its conceptual simplicity and its capability to handle complicated geometry and variability
106 patterns without requiring over-simplified assumptions. A number of works based on
107 Monte Carlo simulation have yielded a full description of the shearing processes and the
108 probability of failure or the reliability of fully saturated heterogeneous slopes (Griffiths
109 and Fenton 2004; Griffiths and Marquez 2007; Hicks and Onisiphorou 2005; Hicks and
110 Samy 2002).

111 There have been a number of studies investigating the influence of rainfall intensity,
112 water table and permeability on the stability of saturated slope (e.g., Tsaparas et al.
113 (2002)). The main findings from these works cannot be directly applied to unsaturated
114 slopes, because the flow characteristics in unsaturated soils are different from the ones
115 observed under saturated conditions. Past studies on unsaturated slope stability are mostly
116 limited to homogeneous soil properties and were conducted using different approaches,
117 including analytical solution, the LEM and the FEM. Griffiths and Lu (2005) and Lu and
118 Godt (2008) suggested a formula based on suction stress that takes into account both, the
119 soil characteristics and the infiltration rate. The suction stress was then used to
120 analytically predict the stability of an infinite unsaturated slope in a steady seepage
121 condition. Ng and Shi (1998) conducted a LEM parametric study to investigate the effect
122 of various hydraulic parameters, amongst others: permeability, rainfall intensity,
123 infiltration duration and boundary conditions. It was observed that soil permeability and
124 rainfall characteristics (i.e. intensity and duration) could have significant influences on
125 the stability of unsaturated slopes. Importantly, the factor of safety can reduce
126 considerably with the relative differences in magnitude between the soil permeability and
127 the rainfall intensity and it might also depend on permeability anisotropy.

128
129

130 Few studies have also attempted to incorporate material uncertainties into a stochastic
131 analysis of partly saturated slopes. Among these studies, some are limited to the analysis
132 of infinite slopes with one-dimensional random variations of permeability (Santoso et al.
133 2011; Dou et al. 2014; Cho and Lee 2001; Cho 2014; Xia et al. 2017). For example, Dou
134 et al. (2014) employed a Green-Ampt infiltration model to obtain a closed form of the
135 limit state function of an infinite slope. The Monte Carlo simulation method was then
136 used to study the influence of saturated permeability on slope failure during rainfall. Xia
137 et al. (2017) adopted a stochastic method to predict the risk of failure of an infinite
138 unsaturated slope subjected to rainfall. They proposed an analytic solution and compared
139 it against a Monte Carlo simulation.

140

141 Sensitivity analyses looking at the effect of different factors (e.g. slope angle, water table
142 position, soil air entry value, dry density and specific density) on slope failure were also
143 conducted. Zhang et al. (2005) developed a coupled hydro-mechanical finite element
144 model to study the effect of the variability of different constitutive parameters. Zhang et
145 al. (2014) also extended this model to the analysis of rainfall intensity-duration and
146 suggested a framework for predicting time-dependent failure probability. Arnold and
147 Hicks (2010) studied the effect of the random variability of friction angle, cohesion,
148 porosity, saturated permeability and air entry suction on the stability of a finite
149 unsaturated slope. Phoon et al. (2010) proposed a probabilistic model of normalised soil
150 water retention curve (SWRC), whose shape and air entry value were modelled by a
151 correlated lognormal vector. The study did not however take into account the variability
152 of saturated permeability. Santoso et al. (2011) further developed the SWRC model
153 proposed in Phoon et al. (2010) by incorporating the saturated water content as an
154 additional random variable. The Kozeny-Carman equation was adopted to link the
155 random saturated water content to the saturated permeability. This approach implies that
156 the shape of the SWRC and the saturated permeability are independent from one another,
157 while in the present study they are coupled through the porosity as described later.

158

159 A limited number of authors have also investigated the depth of the failure zone. Alonso
160 and Lloret (1983) showed that the slope angle marking the transition from shallow to

161 deep failure increases with soil dryness. Hicks et al. (2008) presented a three-dimensional
162 stochastic study of the size of the sliding area in saturated slopes. Santoso et al. (2011)
163 demonstrated instead that shallow failure mechanisms in randomly heterogeneous infinite
164 unsaturated slopes cannot be predicted using a homogeneous slope model. Finally, Le et
165 al. (2015) evaluated the effect of the standard deviation and correlation length of random
166 porosity on the size of the sliding area in an unsaturated slope.

167

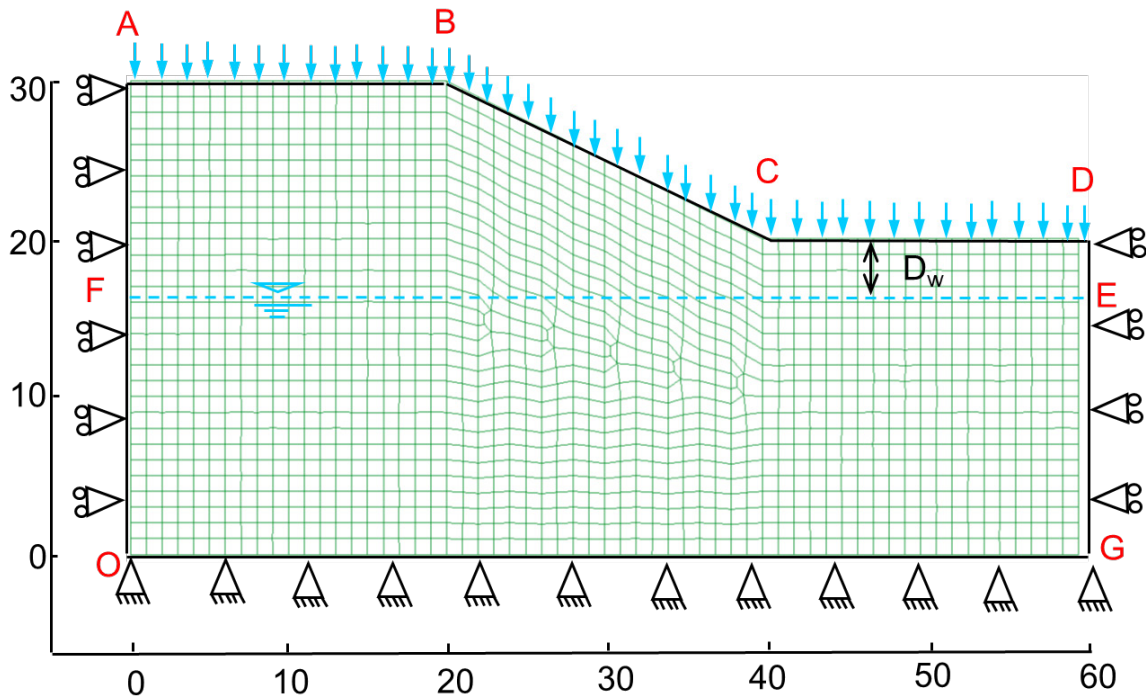
168 Following upon earlier studies, the present work investigates the effect of external and
169 internal factors on the uncertainty of the factor of safety and failure size in unsaturated
170 slopes with randomly heterogeneous porosity. These factors include external
171 environmental conditions (i.e. water table depth and rainfall intensity) and internal soil
172 parameters (i.e. saturated permeability and water retention characteristics). Importantly,
173 unlike random saturated soils, preferential water pathways do not necessarily coincide
174 with the most porous regions (Le et al. 2015). These regions might in fact exhibit smaller
175 values of permeability because of lower saturation levels. A fully coupled hydro-
176 mechanical FE code is adapted to perform the numerical simulations involving a finite
177 slope. The Monte Carlo method is adopted to conduct the probabilistic study.

178

179 **2 Method**

180 **2.1 Model geometry**

181



182

183

184

185

186 Figure 1: Slope dimensions and boundary conditions (scale in meters)

187

188 The numerical model adopted in the present analysis consists of a slope with a 2:1
 189 gradient discretized into a finite element mesh of 1515 quadrilateral elements with four
 190 integration point and an average area of $\sim 1\text{m}^2$ (Figure 1). The finite element
 191 CODE_BRIGHT software (Olivella et al. 1996; UPC 2010) was adopted to conduct the
 192 numerical analyses. This software allows fully coupled thermo-hydro-mechanical
 193 simulations of boundary value problems in unsaturated soils. Thermal processes are
 194 however not considered in this study, which focuses exclusively on coupled hydro-
 195 mechanical processes.

196

197 A mesh sensitivity analysis was initially performed under saturated conditions, which
 198 confirmed the accurate estimation of the safety factor by the model shown in Figure 1 (Le
 199 2011). The suitability of the mesh was further verified in unsaturated conditions against
 200 commercial software (GEO-SLOPE International Ltd) using the limit equilibrium
 201 method. For a given rainfall, the commercial software produced similar changes of the
 202 factor of safety compared to the adopted finite element model (Le et al. 2015).

203

204 **2.2 Hydraulic and mechanical models**

205 The hydraulic constitutive models adopted in this study are presented in Eqs. 1 to 5:

$$206 \quad S_e = \frac{S - S_r}{S_s - S_r} = \left(1 + \left(\frac{S}{s_e} \right)^{1-m} \right)^{-m} \quad (1)$$

$$207 \quad s_e = s_{e0} \exp(\eta(\phi_o - \phi)) \quad (2)$$

$$208 \quad k_s = k_{so} \frac{\phi^3}{(1-\phi)^2} \frac{(1-\phi_o)^2}{\phi_o^3} \quad (3)$$

$$209 \quad k_r = \sqrt{S_e} (1 - (1 - S_e^{1/m})^m)^2 \quad (4)$$

$$210 \quad \mathbf{q} = -k_s k_r \left(\frac{u_w}{\rho_w g} + z \right) = -k_u \nabla \left(\frac{u_w}{\rho_w g} + z \right) \quad (5)$$

211

212

213 This work employs the van Genuchten (1980) model for the soil water retention curve
 214 (SWRC) (Eq. 1-2), the Kozeny's relationship (Kozeny 1927) between saturated
 215 permeability and porosity (Eq. 3) and the van Genuchten and Nielsen (1985) model for
 216 the unsaturated relative permeability (Eq. 4). The unsaturated permeability k_u is then the
 217 product of the saturated and relative permeabilities (i.e. $k_u = k_s k_r$) while the unsaturated
 218 flow \mathbf{q} is calculated using the generalised Darcy's law (Eq. 5). The above models can
 219 realistically describe unsaturated flow in a simple and numerically stable way, which is
 220 highly desirable when dealing with finite element simulations. Nevertheless, they rely on

221 the simplifying assumption that capillarity dominates the hydraulic regime and that other
222 forces linked to adsorptive phenomena are negligible.

223

224 The SWRC (Eq. 1) relates the effective degree of saturation S_e to suction s through the air
225 entry suction parameter s_e and the retention gradient m (van Genuchten 1980). The value
226 of S_e is calculated as a function of the current degree of saturation S , the maximum degree
227 of saturation S_s , and the residual degree of saturation S_r . The effect of heterogeneity is
228 introduced by relating the parameter s_e to porosity ϕ through the parameter η (Eq. 2) that
229 controls the rate at which s_e deviates from its reference value s_{e0} when ϕ deviates from its
230 reference value ϕ_0 (Rodríguez et al. 2007; Zandarín et al. 2009). Similarly, Kozeny's
231 equation (Eq. 3) describes the deviation of the saturated permeability k_s from its reference
232 value k_{s0} when ϕ deviates from its reference value ϕ_0 (Kozeny 1927). The van Genuchten
233 and Nielsen (1985) permeability curve (Eq. 4) relates instead the relative permeability k_r
234 to the effective degree of saturation S_e , and therefore indirectly to porosity ϕ , through the
235 gradient m of the SWRC curve. The symbols u_w , ρ_w , g and z indicate the pore water
236 pressure, the water density, the gravitational acceleration and the elevation coordinate,
237 respectively. The water retention behaviour and permeability are therefore spatially
238 heterogeneous which influences the hydraulic processes within the soil masses . More
239 details about these relationships can be found in UPC (2010).

240

241 Unless otherwise stated, the base values of m , k_{s0} , s_{e0} and η are constant and equal to the
242 values shown in Table 1. These values are about the middle of their respective typical
243 range of variation (i.e. those values that are physically possible and are of interest in
244 practically applications) to avoid unrepresentative results (Bear 1972; van Genuchten
245 1980; Zandarín et al. 2009). The base value of $k_{s0}=10^{-5}$ m/s lies in the upper permeability
246 range of layered clays or clayey silts. The choice of a relatively high k_{s0} facilitates
247 numerical simulations by easing the steep change of pore pressure across the wetting
248 front. During the sensitivity analysis, the parameters k_{s0} , η and m are varied in their
249 typical range to investigate the effect on slope stability. In Eq. 1, the values of S_s and S_r
250 are equal to 1 and 0.01, respectively.

251

252 A linear elastic model with an extended Mohr-Coulomb (MC) failure criterion (Eq. 6) is
253 adopted to simulate the mechanical behaviour of the unsaturated soil (Fredlund et al.
254 1978):

255

$$256 \quad \tau = c' + \sigma \tan \phi' + s \tan \phi^b \quad (6)$$

257

258 Eq. 6 reflects the dependency of the shear stress at failure τ on net normal stress σ and
259 suction s through the effective friction angle ϕ' , effective cohesion c' and a parameter
260 controlling the increase in shear strength with suction ϕ^b . The cohesive component of
261 strength provided by suction (i.e. the 3rd term in Eq. 6) reduces with decreasing s and
262 becomes zero for a fully saturated soil (i.e. $s = 0$). In reality, the value of ϕ^b has been
263 shown experimentally not to be constant but to decrease with increasing s (Escario and
264 Saez 1986; Gan et al. 1988) starting from ϕ' in saturated conditions. In particular, Gan et
265 al. (1988) suggested that, as the soil desaturates, the value of ϕ^b decreases up to a
266 relatively constant value. For simplicity, however, this study assumes a constant value of
267 ϕ^b .

268

269 The assumed values of c' , ϕ' and ϕ^b are typical of clays and are based on those reported
270 by Bishop et al. (1960) for boulder clay and by Gan et al. (1988) for a compacted glacial
271 till. The elastic parameters (i.e. Young's modulus E and Poisson's ratio ν), are also
272 related to typical values observed in clayey soils, and chosen within their respective
273 ranges (Zhu 2014). The variation of porosity may also influence mechanical behaviour,
274 but this aspect is not considered in this study. The mechanical parameters are therefore
275 assumed to be homogeneous (spatially uniform) and are set equal to the values listed in
276 Table 1. This assumption facilitates the investigation of the effect of porosity
277 heterogeneity on the hydraulic behaviour by isolating it from other effects.

278

279 A non-associated flow rule with zero dilatancy is assumed, which means that no plastic
 280 volumetric strains occur during yielding. Moreover, a viscoplastic integration algorithm
 281 is used to update the stress field during plastic loading (Olivella et al. 1996).

282

283 Table.1: Base values of soil parameters adopted in the numerical analyses

Hydraulic model			Mechanical model		
Symbol	Units	Value	Symbol	Units	Value
m		0.2	E	kPa x 10 ³	100
η		5	ν		0.3
ϕ_o		0.333	ϕ'	°	20
k_{so}	m/s	10 ⁻⁵	c'	kPa	5
s_{eo}	kPa	20	ϕ^b	°	18

284

285 As shown in Eq. 6, $\tan\phi^b$ controls the increase in shear stress at failure with suction,
 286 which provides an additional source of cohesive strength with respect to the effective
 287 cohesion c' . Therefore, when implementing the shear strength reduction technique for
 288 estimating the factor of safety (FoS), the same reduction is applied to all strength
 289 parameters (c'_{actual} , $\tan\phi'_{actual}$, $\tan\phi^b_{actual}$) to obtain the corresponding values at failure
 290 (c'_{fail} , $\tan\phi'_{fail}$, $\tan\phi^b_{fail}$) according to the following definition of FoS for unsaturated soils:

291

$$292 \quad FoS = \frac{c'_{actual}}{c'_{fail}} = \frac{\tan\phi'_{actual}}{\tan\phi'_{fail}} = \frac{\tan\phi^b_{actual}}{\tan\phi^b_{fail}} \quad (7)$$

293

294 The use of Eq. 7 in conjunction with the FE program CODE_BRIGHT has been verified
 295 against the Limit Equilibrium Method by using the commercial software SeepW and
 296 SlopeW (GEO-SLOPE International Ltd) and has been shown to produce comparable
 297 values of FoS (Le 2011, Le et al. 2015). More details about the application of the shear

298 strength reduction method using CODE_BRIGHT can be found in Le (2011) and Le et al.
299 (2015).
300

301 **2.3 Boundary conditions and simulation process**

302 At the very start of the analysis, gravity is applied to an initially weightless slope to
303 establish the initial stress distribution due to self-weight. The acceleration of gravity is
304 increased from zero to the standard value of 9.8 m/s^2 over a 'fictitious' time (UPC 2010).
305 The random porosity field is introduced prior to applying gravity, so that the initial stress
306 distribution takes into account the variation of the soil unit weight due to material
307 heterogeneity.

308

309 The initial distribution of pore water pressure p_w is assumed hydrostatic in equilibrium
310 with the water table. The water table is fixed at 5 m below the slope toe, except for those
311 analyses where the effect of water table depth is investigated. The pore air pressure is
312 assumed constant and equal to the atmospheric pressure (i.e. $p_a=0$) and the suction s is
313 therefore equal to the negative value of the pore water pressure (i.e. $s=-p_w$). The initial
314 suction is therefore largest at the crest of the slope AB and equal to $s_{max}=150 \text{ kPa}$ under
315 hydrostatic conditions. This level of surface suction is typically encountered in arid or
316 semi-arid countries such as Australia (e.g., Cameron et al. (2006)). The assumption of an
317 initially hydrostatic pore pressure distribution ignores the potential presence of
318 evaporation at ground level. This simplification is acceptable in the context of this work,
319 whose objective is to analyse the sensitivity of the stability of unsaturated slopes to
320 different parameters rather than describing the hydrological and failure regimes of a real
321 case.

322

323 A rainfall of constant intensity is then applied at the boundary $ABCD$ over 10 days
324 (Figure 1). This boundary condition imposes a constant rate of infiltration into the soil as
325 long as the pore water pressure at the boundary is negative (i.e. as long as suction is
326 positive). If the pore water pressure becomes equal or larger than zero, the boundary
327 condition shifts to a constant zero pore water pressure to avoid the build-up of a hydraulic

328 head at the ground surface. This type of boundary condition is often referred to as a
329 “seepage” boundary condition and is further described in CODE_BRIGTH Users’
330 Manual (UPC 2010) or Le et al. (2012). After 10 days, the rainfall is stopped and the
331 boundary $ABCD$ is assumed impermeable but the simulation is continued for another 355
332 days to allow the redistribution of pore water pressure back to a hydrostatic condition.
333 The boundaries OA , OG and GD are assumed impermeable during and after the rainfall,
334 which causes the infiltrated water to accumulate inside the soil domain and the water
335 table to rise. This describes a situation in natural slopes where surrounding soils have low
336 permeability or neighbouring areas have poor drainage capacity (e.g., due to a blocked
337 drain). Such a condition can indeed be critical for slope stability in reality. If evaporation
338 and/or dissipation were allowed, the water table position would be affected depending on
339 the considered assumptions. For example, if high rates of evaporation are assumed the
340 rise of the water table will be strongly affected, leading to an eventual little water
341 accumulation in the slope domain and therefore to a practically stable position of the
342 water table during the rainfall. Then, the changes of the safety factor and size of failure
343 mass during the rainfall would be less than the results obtained in this study. In addition,
344 the values of these parameters after the rainfall would be almost the same as at the
345 beginning of the rainfall. Similar reasoning can be used with respect to the inclusion of
346 dissipation in the simulations. The mechanical boundary conditions are also indicated in
347 Figure 1.

348

349 The Monte Carlo analysis involves the generation of multiple random porosity fields that
350 are mapped onto the FE mesh shown in Figure 1. These FE meshes with different
351 random porosity fields constitute the “realisations” of the Monte Carlo analysis. Each
352 realisation is analysed in two consecutive stages corresponding to: *i*) the calculation of
353 the pore water pressure and stress fields at distinct times during or after the rainfall; and
354 *ii*) the application of the shear strength reduction technique (SRT) to the calculated pore
355 water pressure and stress fields to determine the factor of safety (FoS) and sliding area
356 (A_s) at a given time.

357

358 Note that, in stage *i*), soil deformations are fully coupled with pore water flow and the
359 equations of equilibrium and hydraulic continuity are solved simultaneously in
360 CODE_BRIGTH. The nonlinear equations associated with flow and mechanical
361 problems are solved in a fully coupled manner using the New-Raphson method (Olivella
362 et al., 1996). This implies that as the rainfall seeps into the unsaturated soil, suction
363 (and/or positive pore water pressure) changes will induce net (or effective) stresses
364 changes. This in turn induces deformations in the soil elements. These deformations
365 cause changes in the soil porosity, which lead to changes in intrinsic permeability and air
366 entry value through equations 2 and 3, respectively. The new permeability and air
367 entry value influence the water flows through equation 1, 4 and 5. The
368 unsaturated/saturated flow and the mechanical deformations are therefore truly coupled.

369

370 Eight points in time are selected to extract the corresponding fields of stresses and pore
371 water pressure to be used in the subsequent shear strength reduction stage. These include
372 four times during the rainfall (i.e. 0, 0.5, 5, 10 days) and four times after the rainfall (i.e.
373 15, 20, 100 and 365 days). The selected times aim at capturing the changes in the failure
374 mechanism associated with a significant variation of the pore water pressure p_w field.

375

376 Note that the *SRT* analysis is simply a numerical technique used in stage *ii*) to estimate
377 the factor of safety FoS and sliding area A_s corresponding to the field of stresses and pore
378 water pressures calculated at a given time. During a *SRT* analysis, the calculated pore
379 water pressures field is fixed at every mesh node while the calculated stresses and strains
380 fields are imposed as initial conditions. The shear strength parameters are then reduced
381 by a factor that is initially equal to one and subsequently augmented in steps of 0.01 until
382 failure. Failure corresponds to the detection of significant movements on the slope
383 surface. The value of the reduction factor at this point is assumed to coincide with the
384 FoS of the slope (Eq. 7). Note that the above methodology allows the natural
385 development of the slip surface through the weakest path within the soil domain, which is
386 an advantage compared with limit equilibrium methods where the shape of the slip
387 surface is instead assumed. Le et al. (2015) provided detailed explanation of the criteria
388 used to detect the failure mechanism.

389

390 After failure, the number of mesh nodes that have moved substantially is counted to
391 compute the sliding area of the slope (Le et al. 2015). One node corresponds to a region
392 that is the sum of one quarter of each of the four elements sharing that node. Since the
393 mesh mostly consists of square or parallelogram elements of 1 m^2 (Figure 1), the area
394 allocated to each node is approximately 1 m^2 and the number of “failed” nodes provides a
395 reasonably good estimation of the sliding area A_s in m^2 . This is clearly an approximation
396 because the nodes on the boundary of the failed region contribute less area than the inner
397 nodes. Nevertheless, this approximation is considered acceptable as the present study
398 focuses on a sensitivity analysis rather than on the accurate determination of the sliding
399 area. For real slopes, it is recommended that A_s is estimated more accurately either by
400 using a finer mesh or by directly measuring the area of the failed region.

401 **3 Random porosity field**

402 Porosity ϕ is probably one of the most easily measured soil parameters exhibiting spatial
403 variability (Le et al. 2013). Porosity values are theoretically bounded between 0 and 1,
404 thus they should be represented by a bounded random distribution such as the tanh-
405 bounded function. This distribution requires 4 parameters which are a lower bound, an
406 upper bound, the location parameter (equal to 0 when random variable is symmetric
407 about the midpoint of the variable range) and a scale parameter which increases with
408 increasing level of variability. The bounded distributions are mathematically complex so
409 a different approach is employed in the present work by generating an univariate random
410 field of void ratio e instead of porosity ϕ . The void ratio can take any positive value and
411 may thus be modelled by a log-normal probability function (Baecher and Christian 2003;
412 Lacasse and Nadim 1996). The generated random field of void ratio is then converted
413 back into a random field of porosity by using the relationship $\phi=e/(1+e)$. This equation
414 implies that the random field does not generate any value of porosity equal to zero. Such
415 a value is considered unrealistic for the size of the mesh considered in this study.

416

417 Random fields of void ratio are produced by using the Local Average Subdivision (LAS)
418 algorithm and the Markov auto-correlation function (Fenton 1990). The Local Average
419 Subdivision (LAS) method (Fenton, 1990) involves a recursive subdivision process. The
420 original domain is first subdivided into equal sized area, then each area is divided again
421 into smaller areas and this process keeps going until the desirable resolution is achieved.
422 At every stage of subdivision, random values are generated for each area with the
423 variance and covariance structure inherently related to the size of the subdivided area
424 relative to the original domain. Both the LAS algorithm and the Markov function have
425 already been used in geotechnical engineering (Fenton 1990; Griffiths and Fenton 2004).
426 The random field is generated over a regular grid covering a rectangular area with
427 dimensions equal to the largest width and height of the soil domain. The grid is then
428 superimposed on the finite element mesh, so that the bottom left corners of the grid and
429 mesh coincide. An algorithm is subsequently executed to identify the cell in the random
430 field grid with the closest centroid to the centroid of each finite element. The void ratio of
431 the finite element is then taken to coincide with the random value of that cell. Le (2011)
432 explains in detail the procedure to verify that statistical parameters are correctly
433 transferred in the above mapping process.

434

435 The effect of the statistical parameters governing the random distribution of void ratio e
436 (i.e. mean $\mu(e)$, standard deviation $\sigma(e)$ and correlation length $\theta(e)$) were studied in detail
437 in Le et al. (2015). In this study, the values of the mean $\mu(e)$, coefficient of variation
438 $COV_e = \sigma(e)/\mu(e)$ and correlation length $\theta(e)$ are therefore kept constant and equal to 0.5,
439 0.8 and 8 m, respectively (which correspond to $\mu(\phi) = 0.3$, $COV_\phi = 0.46$ and $\theta(\phi) = 8$ m).
440 The effect of COV_e and $\theta(e)$ has been investigated in another study (Le et al. 2015). The
441 chosen values for COV_e and $\theta(e)$ aim to avoid too large or too small effect of these
442 parameter on the results, and increase the possibility of observing the effect of porosity
443 heterogeneity on suction distribution within the slope.

444

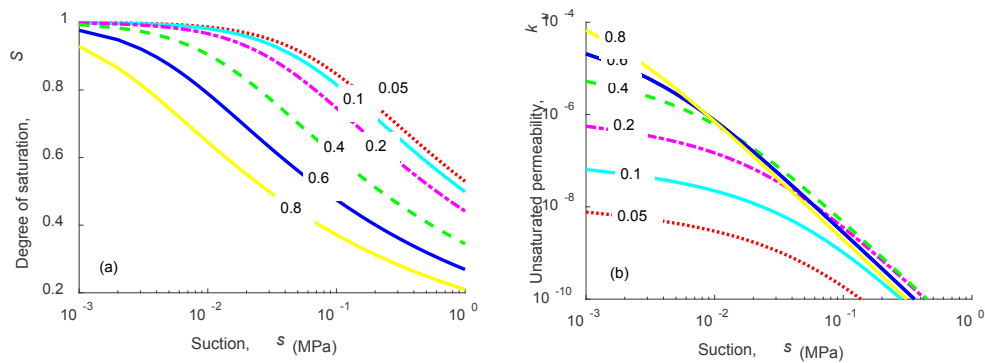
445 Figures 2a and 2b show the influence of porosity on the SWRC and k_u curves alculated
446 using Eqs. 1-4 and the input parameters are listed in Table 1. Six values of porosity, from
447 0.05 to 0.8, are considered. A value of porosity outside this range is quite unlikely

448 considering the coefficient of variation adopted in this study. Based on Figure 2a, the
449 initial degree of saturation near the crest of the slope (i.e. $s \approx 150$ kPa) varies between 0.3
450 and 0.8 with a corresponding value of k_u in the range 10^{-10} – 10^{-9} m/s.

451

452 A heterogeneous porosity field therefore generates non-uniform distributions of degree of
453 saturation and permeability (in addition to a non-uniform distribution of specific weight),
454 which leads to an irregular advancement of the wetting front and an uneven distribution
455 of pore water pressures. This affects the distribution of shear strength, which is controlled
456 by pore water pressure (in addition to the distribution of stresses, which is governed by
457 the overburden weight) and has an impact on the factor of safety of the slope as well as
458 on the size of the sliding mass.

459



460

461 Figure 2. Influence of porosity on the variation of degree of saturation (a) and unsaturated
462 permeability (b) with suction.

463 Noticeably, the degree of saturation (Figure 2a) decreases with increasing porosity while
464 the unsaturated permeability (Figure 2b) increases with increasing porosity. The latter
465 (i.e. k_u) is however little affected when suction is above 20 kPa and the porosity is higher
466 than 0.2. This implies that, in unsaturated soils, the higher porosity regions are not
467 necessarily the most permeable ones, as it is instead the case in saturated soils.

468

469 **4 Influence of hydraulic characteristics**

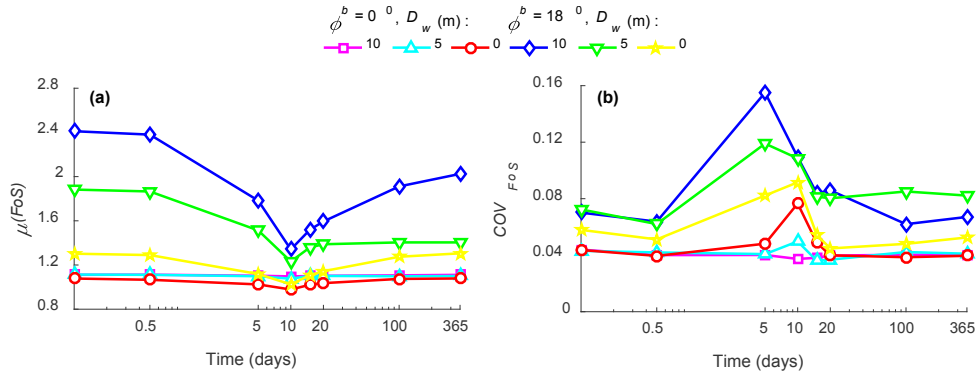
470 **4.1 Water table depth**

471 The initial suction of the soil affects both its degree of saturation and unsaturated
472 permeability (Eqs. 1 and 4), which makes the initial position of the water level (D_w) an
473 important factor to consider. Three values of water table depth measured with respect to
474 the toe of the slope are investigated in this section, namely 0, 5 and 10 m. Under
475 hydrostatic conditions, these depths correspond to the three maximum values of initial
476 suction at the crest of the slope of 100, 150 and 200 kPa, respectively. For each depth,
477 two analyses are compared: one considering the effect of suction on shear strength, i.e.
478 $\phi=18^\circ$, and one neglecting this effect, i.e. $\phi=0$.

479 The evolution of the mean and coefficient of variation of FoS , i.e. $\mu(FoS)$ and COV_{FoS} ,
480 are presented in Figures 3a and 3b, respectively. When the effect of suction is considered
481 (i.e. $\phi=18^\circ$), the $\mu(FoS)$ progressively decreases during the rainfall, because of the
482 reduction in shear strength triggered by the reduction of suction in the unsaturated region
483 but also because of the build-up of positive pore water pressures in the saturated area at
484 the slope toe. In all the analyses, the lowest value of $\mu(FoS)$ occurs just before the end of
485 the rainfall. The $\mu(FoS)$ then recovers over the post-infiltration period (i.e. day 10 to 365),
486 because of the suction increase caused by the downward drainage and the consequent
487 dissipation of positive pore water pressure. The final $\mu(FoS)$ values (i.e. at day 365) are
488 lower than the initial ones because of the rise of water table induced by the accumulation
489 of infiltrated water.

490

491 For the case of $\phi=18^\circ$, the $\mu(FoS)$ consistently increases with increasing D_w because of
492 the increase in shear strength with growing suction. As rainfall progresses, the slope with
493 the deepest initial water table (i.e. $D_w=10$ m) loses the largest amount of suction, leading
494 to the most substantial reduction in $\mu(FoS)$ from about 2.4 to 1.3 over the 10 days of the
495 rainfall. Instead, the $\mu(FoS)$ of the slope with the shallowest initial water table (i.e. $D_w=0$
496 m) reduces much less from about 1.3 to 1.0 over the same time.

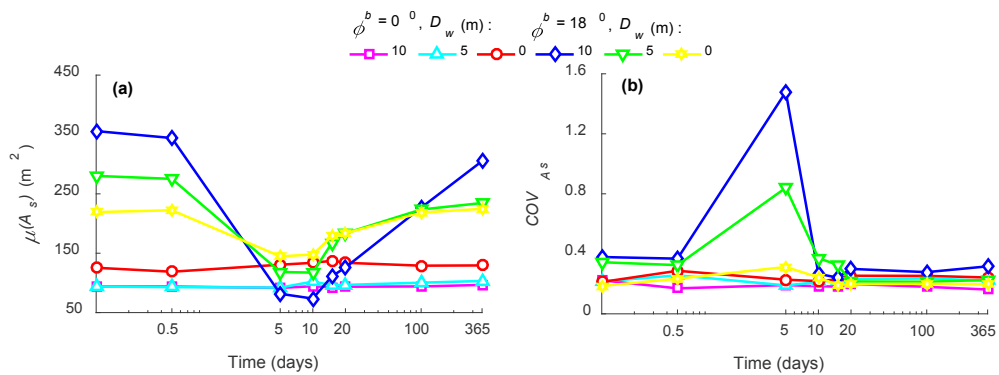


497

498 Figure 3: Time evolution of FoS in terms of mean (a) and coefficient of variation (b).

499 Analyses: influence of water table depth D_w .

500



501

502 Figure 4. Time evolution of A_s in terms of mean (a) and coefficient of variation (b).

503 Analyses: influence of water table depth D_w .

504 Similar results are shown in Figures 4a and 4b but in terms of $\mu(A_s)$ and COV_{A_s} ,

505 respectively. When the effect of suction is included ($\phi^b=18^\circ$), the value of $\mu(A_s)$

506 consistently decreases during the rainfall (though at different rates depending on the D_w

507 value) and reaches a plateau between 5 and 10 days before increasing again during the

508 post-infiltration period. The reason behind this behaviour is that, at the start of the

509 rainfall, the shallow soil region exhibits considerable strength arising from the high

510 suction, which 'pushes' the slip surface to deeper layers in the search of a 'weak' path

511 (Figure 5). However, after a rainfall time between 5 and 10 days, the shallow soil

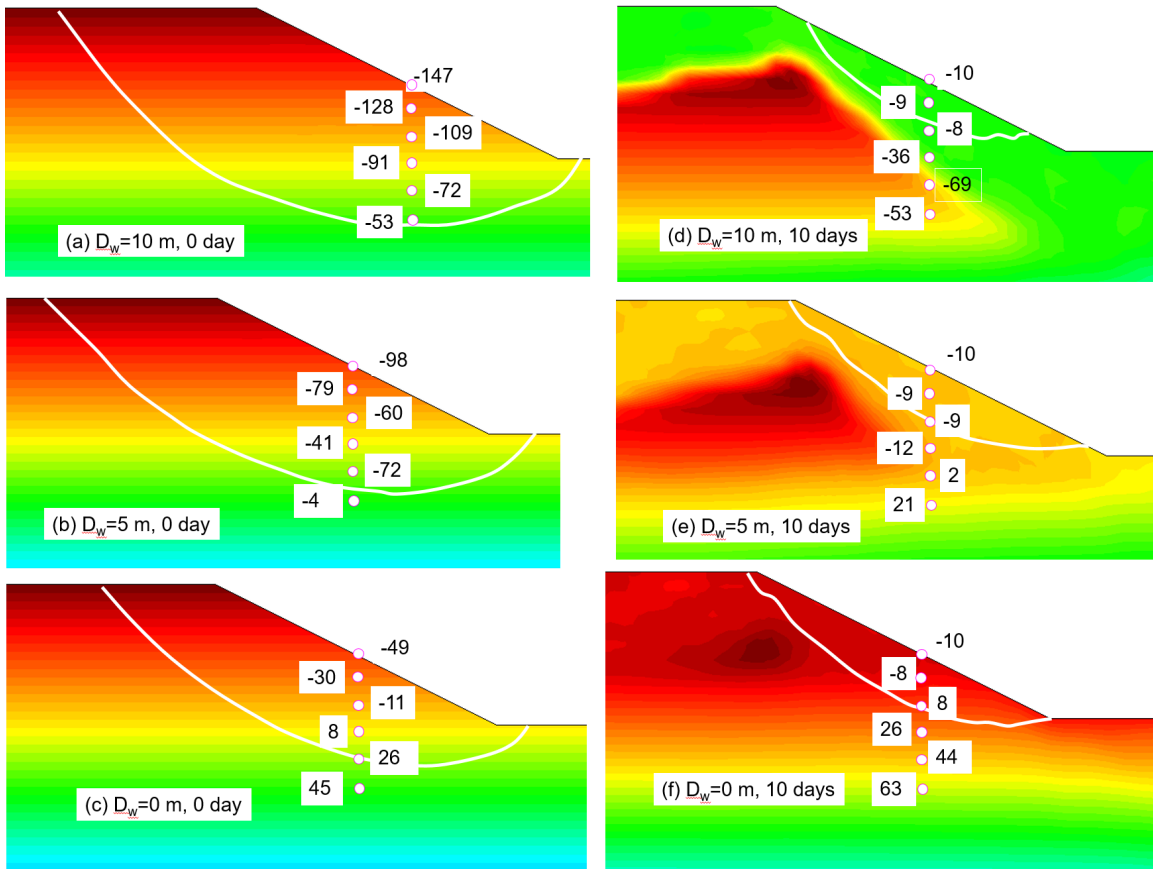
512 experiences a dramatic loss of suction and therefore becomes significantly weaker than

513 the deeper soil. This in turn promotes the formation of a slip surface through the wetted

514 shallow soil layer, which explains why A_s tends to decrease (Figure 5b, 5d, 5f).

515

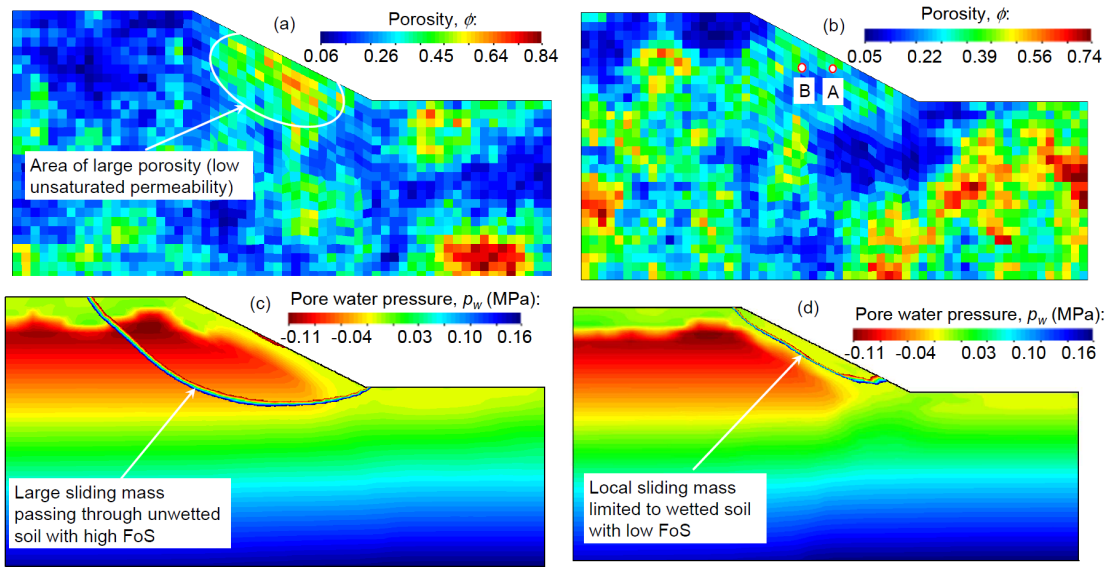
516 For the case of $\phi^b=18^\circ$, the values of $\mu(A_s)$ are higher for larger values of D_w , both at the
517 beginning (i.e. 0 to 0.5 day) and at the end (i.e. 100 to 365 days) of the analysis, because
518 of the larger soil suction associated to a depressed water table (Figure 5a, 5c and 5e).
519 During the course of the rainfall, the wetted area decreases in depth with increasing D_w
520 because of the higher initial suction, and hence the lower degree of saturation and
521 permeability, which delays water infiltration (Figure 5b, d and f). This explains the higher
522 value of $\mu(A_s)$ with smaller D_w between 5 and 10 days (Figure 4a).



523

524 Figure 5. Contour maps of p_w and slip surfaces for different D_w at different times
525 ($\phi^b=18^\circ$). The p_w values shown in labels are in kPa. The p_w colour scale is not the same
526 for all contour plots.

527



528

529 Figure 6: Porosity distributions of sample realisations with significantly different failure
 530 mechanisms (a, b) and contour maps of p_w with sliding surfaces at 5 days (c, d). Results
 531 correspond to $\phi^b=18^\circ$ and $D_w=5$ m.

532 For the case of $\phi^b=18^\circ$, the sliding area at 5 days varies over a wide range of values
 533 depending on the depth of the wetting front in each realisation. There appears to be a
 534 'critical' depth such that, when the wetting front moves below it, the sliding area is
 535 confined to the superficial wetted region (Figure 6b and 6d). In this case, the FoS tends to
 536 be low, because the suction of the 'wetted' elements is relatively low (Figure 56d).
 537 Conversely, if the wetting front is shallower than the 'critical' depth, the slip surface tends
 538 to be deep seated (Figure 6c), like at the start of the rainfall, with a large FoS due to the
 539 high suction along the slip surface. This case might correspond to the existence of a low
 540 permeability layer that prevents the advancement of the wetting front (Figure 6a). The
 541 equal occurrence of both these two extremes (i.e. shallow versus deep slip surfaces)
 542 causes the large values of COV_{FoS} and COV_{As} at 5 days. At 10 days, the wetting front is
 543 likely to have passed the 'critical' depth and hence the majority of slip surfaces is
 544 confined to the superficial wetted region, which explains the consistent decrease in
 545 COV_{FoS} and COV_{As} . An exception to this behaviour is the COV_{FoS} for the case of $D_w=0$ m,

546 which peaks at 10 days because of the dominant destabilizing effect of positive pore
547 pressure build-up at the slope toe.

548 The peak values of COV_{FoS} and COV_{As} significantly increase with increasing D_w implying
549 that the factor of safety and the size of the sliding area become more variable between
550 realisations. After the peak, the values of COV_{FoS} and COV_{As} decrease because of water
551 drainage causing an increase of suction in the unsaturated region and a dissipation of
552 positive pore pressures in the saturated region, which reduce the difference between
553 realisations.

554

555 When the effect of suction on shear strength is not considered (i.e., $\phi^b=0$), Figure 3 shows
556 that the $\mu(FoS)$ is virtually constant for all three D_w values, with only a slight decrease at
557 day 10 for $D_w=0$, while the COV_{FoS} increases slightly with decreasing D_w between 5 and
558 20 days. The build-up of positive pore water pressures with decreasing D_w is the main
559 reason behind this trend given that a larger portion of the slip surface passes through the
560 saturated region as the initial water table is shallower. Figure 4 shows that $\mu(A_s)$ and
561 COV_{As} remain fairly constant over time. Inspection of displacement contours (not shown
562 here) reveal that the sliding areas are very similar for $D_w=5$ m and $D_w=10$ m and do not
563 practically change over time. When the water table is at the ground surface, sliding areas
564 tend to be slightly larger due to the additional stabilizing effects provided by the weight
565 of water in the saturated part of the slope.

566

567 Similar patterns of variation with time of the mean and coefficient of variation of both
568 FoS and A_s were observed in all cases hereafter, hence they will not be discussed further.
569 The comments will instead focus on the sensitivity of the results to the parameters under
570 study.

571 **4.2 Saturated permeability**

572 The reference saturated permeability k_{so} controls the infiltration rate and influences the
573 advancement of the wetting front together with the distribution of pore water pressures. A
574 range of realistic k_{so} values, from 10^{-4} m/s (e.g. pervious well sorted sands) to 10^{-7} m/s

575 (e.g. silts or layered clays), is investigated in this section to gain insights into the
576 influence of this parameter on slope stability.

577

578 Figure 7 and Figure 8 show similar variations of $\mu(FoS)$, $\mu(A_s)$, COV_{FoS} and COV_{A_s} over
579 time as observed in the previous section, except for the lowest value of the reference
580 permeability (i.e. $k_{so}=10^{-7}$ m/s). In this case, almost no water infiltrates the soil and all
581 curves remain practically flat over the entire simulation period.

582

583 Notably, the variation of $\mu(FoS)$ and COV_{FoS} with k_{so} is not monotonic (Figure 7) and the
584 intermediate value of k_{so} (i.e. 10^{-5} m/s) causes the largest average drop of factor of safety
585 as well as the widest variability between realisations (i.e. lowest $\mu(FoS)$ and highest
586 COV_{FoS} for the period 5 to 10 days). This is because the highest value of k_{so} (i.e. 10^{-4} m/s)
587 facilitates water flow leading to smaller gradients of pore pressure together with smaller
588 drops in suction, which results in smaller reductions of shear strength. Conversely, the
589 intermediate value of k_{so} (i.e. 10^{-5} m/s) generates larger gradients of pore pressure with
590 bigger suction drops, which allows the sliding surface to remain inside the wetted region
591 at the surface. This explains the lower values of $\mu(FoS)$ and $\mu(A_s)$ and the higher values of
592 COV_{FoS} and COV_{A_s} for $k_{so}=10^{-5}$ m/s compared to $k_{so}=10^{-4}$ m/s. The evolution of pore
593 water pressures at the two sampling points shown in Figure 9a confirms the larger suction
594 drops at 10 days for $k_{so}=10^{-5}$ m/s compared to $k_{so}=10^{-4}$ m/s (Figure 10).

595

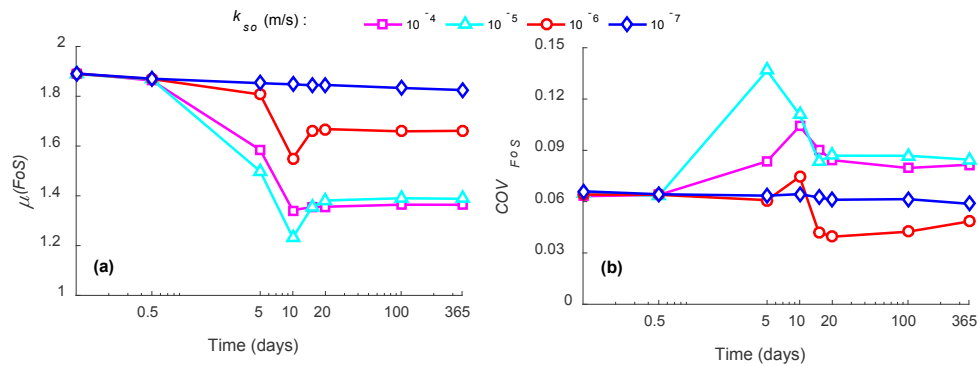
596 The lower value of k_{so} (i.e. 10^{-6} m/s) limits infiltration and restricts the water movement
597 to a very shallow layer along the slope face (Figure 9b). In this case, most of the suction
598 loss is limited to the narrow top region (Figure 10a) while a wider wetted region develops
599 at the slope toe (Figure 9b). Slip surfaces concentrate in this wetted region, which results
600 in smaller values of COV_{FoS} with higher values of $\mu(FoS)$ compared to the previous two
601 cases (Figure 7). Moreover, the value of $\mu(A_s)$ shows a sharp drop at 10 days because of
602 the dominant failure mode cutting through the wetted region above the slope toe (Figure
603 8a). The COV_{A_s} attains a sharp peak at 10 days (Figure 8b) because of the contrast
604 between the majority of realisations predicting a small sliding area constrained to the
605 wetted region and few others predicting a very large value of the sliding area. The latter

606 scenario is observed when the area near the slope toe is dominated by highly permeable
 607 soil.

608

609 The drop of $\mu(A_s)$ and the peak of COV_{A_s} appear earlier (i.e. around 5 days) for the case of
 610 $k_{so}=10^{-5}$ m/s compared to the case of $k_{so}=10^{-6}$ m/s. This is because the soil with $k_{so}=10^{-5}$
 611 m/s is permeable enough to allow the rapid advancement of the wetting front normal to
 612 the slope face. Instead, in the case of $k_{so}=10^{-6}$ m/s, the narrow water path parallel to the
 613 slope face requires a longer time to accumulate enough water at the toe slope for inducing
 614 failure.

615

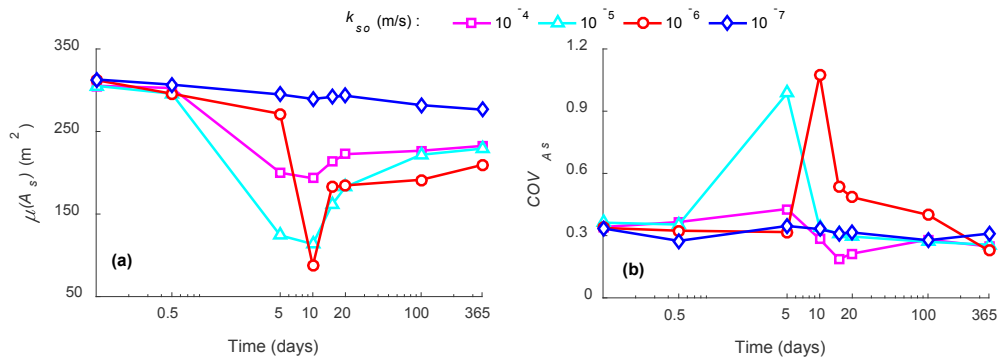


616

617 Figure 7. Time evolution of FoS in terms of mean (a) and coefficient of variation (b).

618 Analyses: influence of reference saturated permeability k_{so} .

619

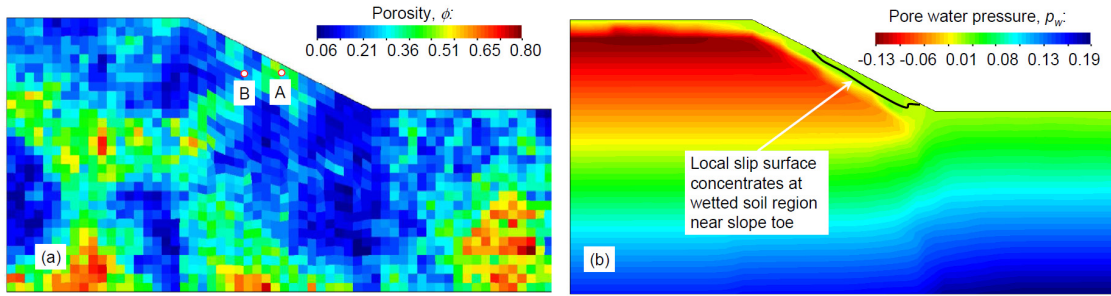


620

621 Figure 8. Time evolution of A_s in terms of mean (a) and coefficient of variation (b).

622 Analyses: influence of reference saturated permeability k_{so} .

623

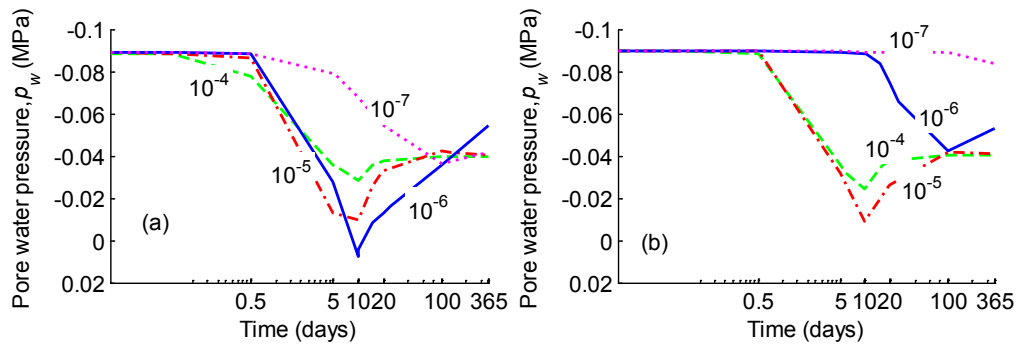


624

625 Figure 9. Porosity distribution of a sample realisation showing sampling points (a) and
 626 contour map of p_w with slip surface at 5 days for the case of $k_{so}=10^{-6}$ m/s (b).

627

628



629

630 Figure 10. Time evolution of p_w for different values of the reference saturated
 631 permeability k_{so} at sampling points A (a) and B (b). Results correspond to the porosity
 632 distribution and sampling points shown in Figure 9a.

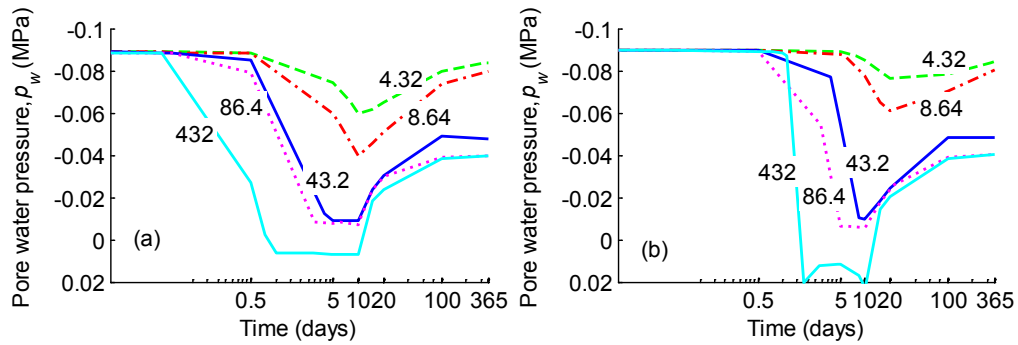
633 4.3 Rainfall intensity

634 The rainfall intensity I_r affects both the amount and rate of water infiltrating into the soil.
 635 To investigate this aspect, five rainfalls of different intensities, from very light (i.e.
 636 $I_r=4.32$ mm/day) to extremely heavy (i.e. $I_r=432$ mm/day), are applied to each realisation
 637 in five separate finite element simulations.

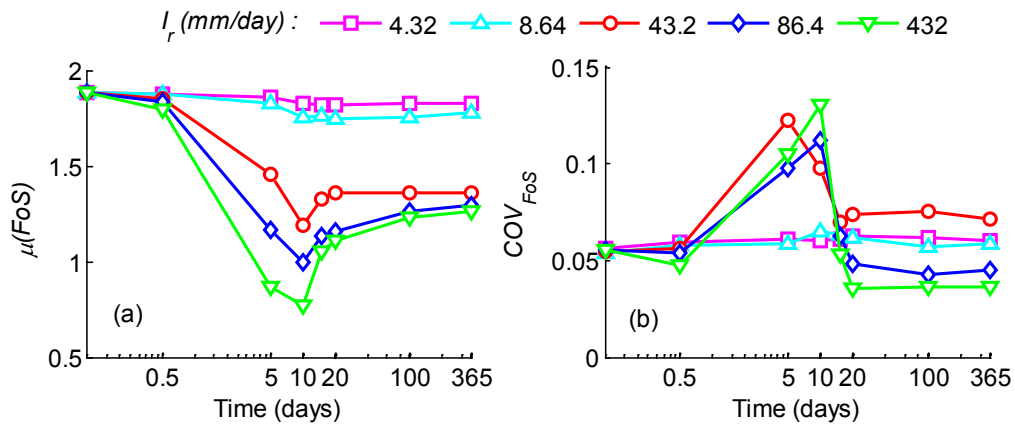
638

639 As expected, the suction drop is more significant for the heavier rainfalls as the amount
 640 of water supply is larger (Figure 11). Therefore, the value of $\mu(ForS)$ generally decreases
 641 with increasing I_r with the most noticeable differences between 5 to 20 days (Figure 12a).

642 The two lighter rainfalls (i.e. $I_r=4.32$ and 8.64 mm/day) do not provide enough water to
 643 induce a substantial change of soil suction, hence the values of $\mu(FoS)$, $\mu(A_s)$, COV_{FoS} and
 644 COV_{A_s} remain approximately constant over time (Figure 12 and Figure 13).
 645

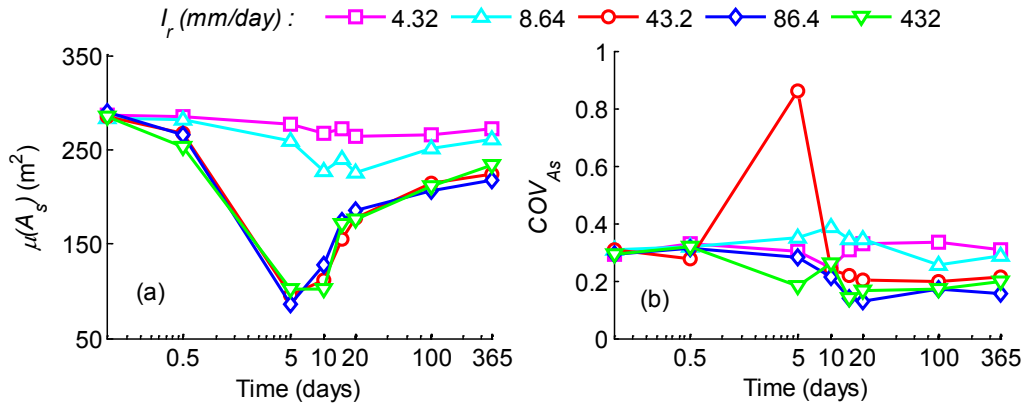


646
 647 Figure 11. Time evolution of p_w for different rainfall intensities I_r at sampling points A
 648 (a) and B (b). Results correspond to the porosity distribution and sampling points shown
 649 in Figure 9a.



650
 651 Figure 12. Time evolution of FoS in terms of mean (a) and coefficient of variation (b).
 652 Analyses: influence of rainfall intensity I_r .

653



654

655 Figure 13. Time evolution of A_s in terms of mean (a) and coefficient of variation (b).

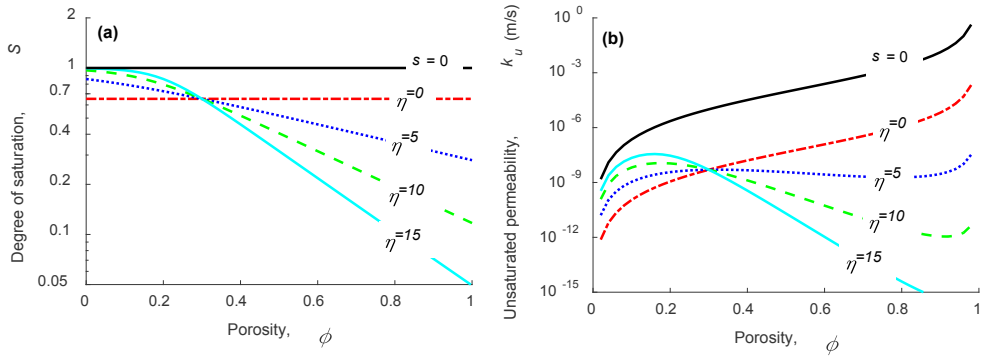
656 Analyses: influence of rainfall intensity I_r .

657 4.4 Soil water retention curve – Parameter η

658 The parameter $\eta > 0$ controls the dependency of the air entry value s_e (Eq. 2) on porosity
 659 and therefore influences the variation of both degree of saturation S (Eqs. 1 and 2) and
 660 unsaturated permeability $k_u = k_r k_s$ (Eqs. 1, 2 and 4) with porosity. Figure 14 shows the
 661 variation of degree of saturation S and unsaturated permeability k_u with porosity ϕ at a
 662 reference suction $s = 100$ kPa for four different values of η , namely $\eta = 0, 5, 10$ and 15 . The
 663 non-monotonic variation of unsaturated permeability k_u (Figure 14b) is the result of the
 664 competition between the growth of saturated permeability k_s (Eq. 3) and the reduction of
 665 relative permeability k_r (Eq. 4) with increasing porosity ϕ . For $\eta = 0$, however, the
 666 variation of unsaturated permeability k_u with porosity ϕ is exclusively governed by the
 667 saturated permeability k_s as the degree of saturation S , and hence the relative permeability
 668 k_r , are independent of porosity. This explains the monotonic variation of k_u for the
 669 particular case where $\eta = 0$ (Figure 14b).

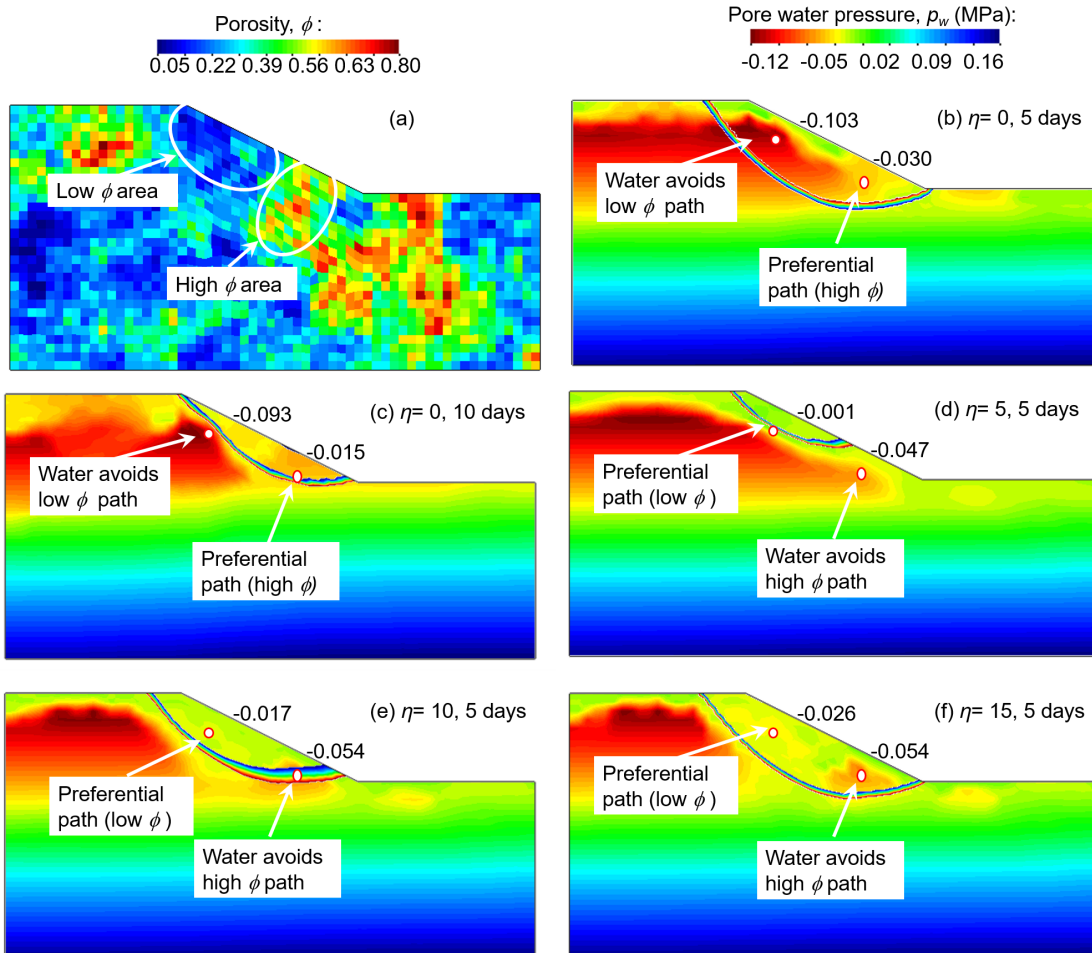
670

671 In Figure 14, the curves for different values of η cross each other at the reference porosity
 672 ϕ_0 , which means that for $\phi > \phi_0$ the degree of saturation S and the unsaturated permeability
 673 k_u increase with increasing η while the opposite is true for $\phi < \phi_0$.



674

675 Figure 14. Variation of S (a) and k_u (b) with η at a reference suction $s=100$ kPa. For the
 676 saturated case (i.e. $s=0$), S and k_u are independent of η .



677

678 Figure 15. Porosity distribution of a sample realisation (a) and corresponding contour
 679 maps of p_w with slip surfaces at different times and for different η values (b, c, d, e, f).

680 For $\eta=5, 10$ or 15 , the reduction of suction caused by rainfall infiltration is more
681 significant in the low porosity regions (i.e. in the upper part of the slope for the
682 realisation shown in Figure 15a) than in the high porosity ones (Figures 15d, 15e, 15f)
683 while the opposite is true for $\eta=0$ (Figures 15b, 15c). This is because, when $\eta=5, 10$ or
684 15 , the water preferentially flows through low porosity regions, i.e. those regions where
685 $\phi < \phi_o$, due to their higher unsaturated permeability (Figure 14b). The opposite is true for
686 the case where $\eta=0$.

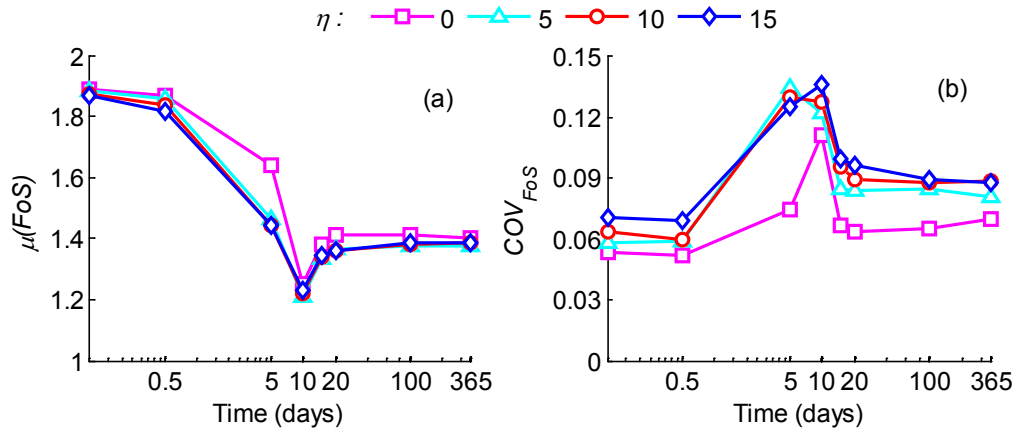
687

688 Figure 16a shows the variation of $\mu(FoS)$ with time, which is almost identical for the
689 three cases where $\eta=5, 10$ or 15 and significantly bigger for the case where $\eta=0$. This
690 pattern is justified by the fact that, in the absence of coupling between porosity and air
691 entry value (i.e. $\eta=0$), water flows preferentially through the higher porosity regions,
692 which require longer times to become saturated. This delays the advancement of the
693 wetting front and explains the higher values of $\mu(FoS)$ for $\eta=0$ compared to $\eta=5, 10$ or
694 15 . The values of COV_{FoS} are also relatively similar for the three cases where $\eta=5, 10$ or
695 15 but significantly smaller for the case where $\eta=0$ (Figure 16b).

696

697 In terms of sliding area, the value of $\mu(A_s)$ decreases with decreasing η , except for the
698 case where $\eta=0$, which exhibits the highest value of $\mu(A_s)$ at 5 days due to the delayed
699 advancement of the wetting front (Figure 17a). The unsaturated permeability k_u exhibits
700 the weakest dependency on porosity ϕ for the case where $\eta=5$ (Figure 14) leading to
701 similar reductions of suction in the superficial wetted region regardless of whether
702 porosity is high or low. This also explains why, in the case of $\eta=5$, suction is lower and
703 full saturation of the top layer is reached at around 5 days (Figure 15d), leading to the
704 formation of smaller sliding areas, i.e. lower values of $\mu(A_s)$ and higher values of COV_{A_s}
705 (Figure 17 b).

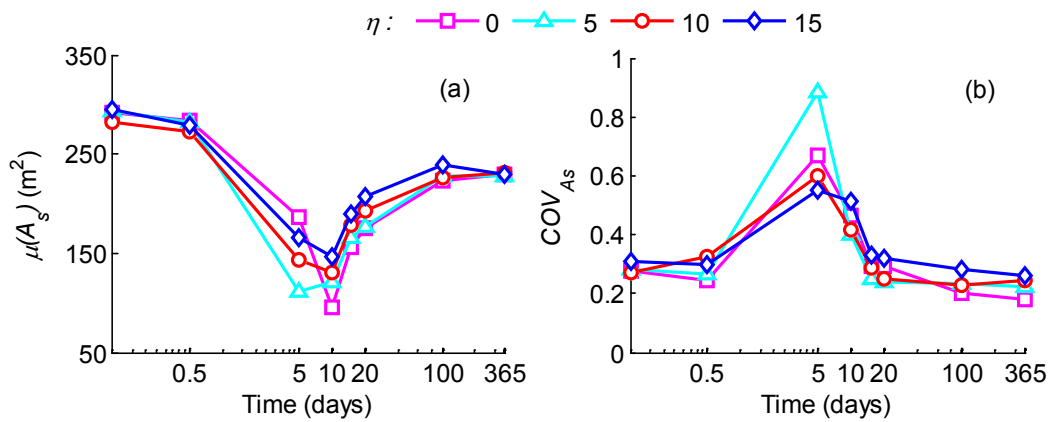
706



707

708 Figure 16. Time evolution of FoS in terms of mean (a) and coefficient of variation (b).

709 Analyses: influence of the SWRC (parameter η).



710

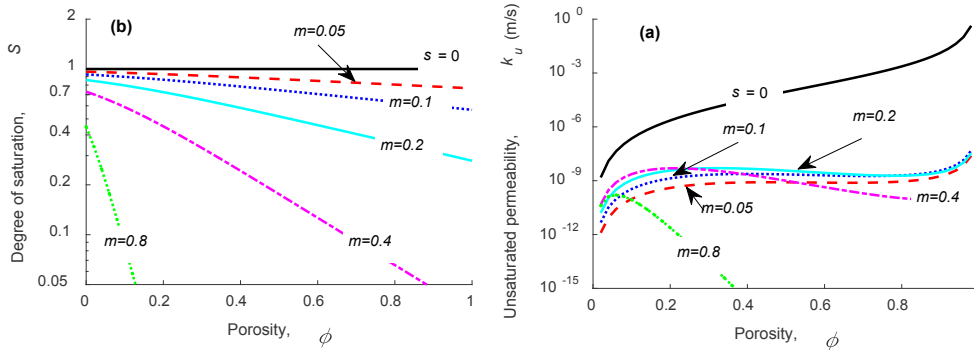
711 Figure 17. Time evolution of A_s in terms of mean (a) and coefficient of variation (b).

712 Analyses: influence of the SWRC (parameter η).

713 4.5 Soil water retention curve – Parameter m

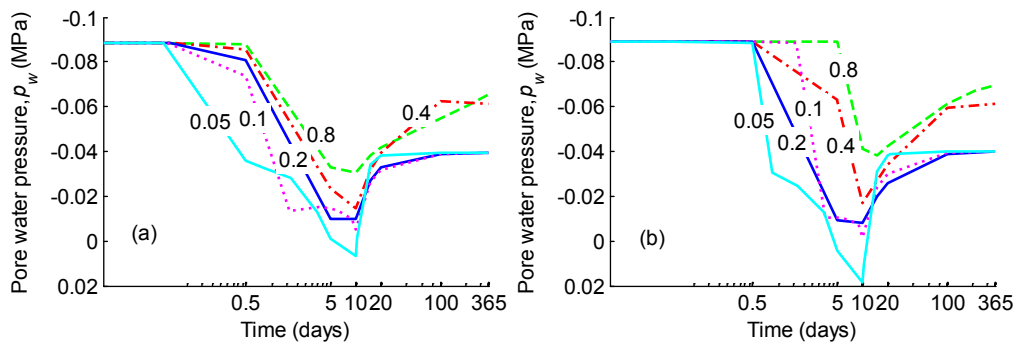
714 The slope of the water retention curve (Eq. 1) becomes more pronounced as the value of
 715 parameter m increases, which results in a decrease of degree of saturation and unsaturated
 716 permeability at a given suction (Eqs. 1 and 4). Figure 18 shows the variation of degree of
 717 saturation S and unsaturated permeability $k_u = k_r k_s$ with porosity ϕ at a reference suction
 718 $s = 100$ kPa for four different values of m , namely $m = 0.05, 0.1, 0.2, 0.4$ and 0.8 . The
 719 variation of k_u with ϕ is relatively modest for $m \leq 0.4$ because of the competing effects of

720 the increase of saturated permeability k_s (Eq. 3) and the decrease of relative permeability
 721 k_r (Eq. 4) with increasing porosity ϕ .



722
 723 Figure 18: Variation of S (a) and k_u (b) with m at a reference suction $s=100$ kPa. For the
 724 saturated case (i.e. $s=0$) S and k_u are independent of m .

725 For a given porosity, if the value of m is small, the soil exhibits a high initial value of S
 726 and therefore requires less water to reach the saturated state (Figure 18a). This produces a
 727 quicker advancement of the wetting front so that an earlier and larger reduction of suction
 728 occurs in the superficial soil layer as shown in Figure 19. This in turn causes an earlier
 729 larger reduction of shear strength, which explains why at the end of the rainfall (i.e. 10
 730 days) the value of $\mu(FoS)$ is about 1.6 for $m=0.8$ but less than 1 for $m=0.05$ (Figure 18a).



731
 732 Figure 19. Time evolution of p_w for different values of parameter m at sampling points A
 733 (a) and B (b). Results correspond to the porosity distribution and sampling points shown
 734 in Figure 6b.

735 In Figure 20b, the value of COV_{FoS} increases with increasing m at initial times (i.e.
 736 between 0 and 0.5 day) because of the increasing variability in overburden weight.
 737 However, the highest COV_{FoS} is achieved at 5 days for an intermediate value of $m=0.2$,

738 which produces the largest spread of failure mechanisms (e.g. Figure 6c and Figure 6d).
739 This is also reflected in the relatively large value of COV_{A_s} . For the larger value $m = 0.4$,
740 the value of COV_{FoS} peaks at 10 days instead of 5 days due to the slower migration of the
741 wetting front compared to the case of $m = 0.2$ as discussed earlier. Similarly, the
742 magnitude of the peak is smaller because most realisations have not reached yet the
743 critical depth. For the smaller values $m = 0.05$ and 0.1 , the wetting front advances faster
744 and is likely to have already passed the critical depth at 5 days. At this time, the vast
745 majority of realisations therefore exhibit sliding areas confined to the top wetted region
746 and correspond, on average, to lower values of FoS and A_s . In this case, the peak of
747 COV_{FoS} at 10 days is caused by the development of a different failure mechanism caused
748 by the rise of the water table in a considerable number of realisations. This higher water
749 table produces the build-up of positive pore pressures and the formation of slip surfaces
750 cutting through the deep saturated region.

751

752 As for the largest value $m = 0.8$, the COV_{FoS} uncharacteristically drops to the lowest value
753 at 10 days (Figure 20b). This is probably due to the fact that the rainfall infiltration
754 reduces the initially large non-uniformity of overburden weight in the unsaturated zone.

755

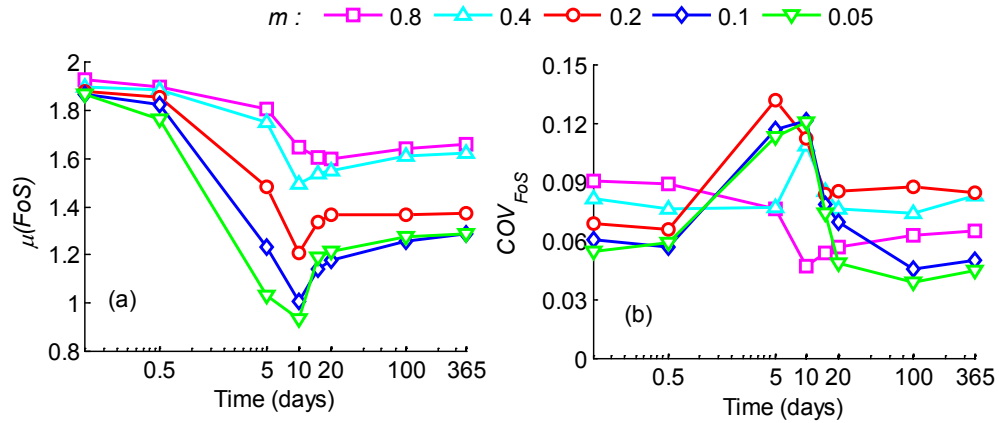
756 The value of $\mu(A_s)$ decreases during the rainfall with the lowest values recorded between
757 5 days for $m = 0.1$ and 10 days for $m = 0.05, 0.2, 0.4$ and 0.8 (Figure 21a). The values of
758 $\mu(A_s)$ for $m = 0.4$ and 0.8 are generally higher than in all other cases because the wetting
759 front did not reach the critical depth in the majority of realisations, which means that the
760 factor of safety and sliding area are generally large.

761

762 The variation of A_s between realisations is marginal for small values of m (i.e. 0.05 and
763 0.1) with no prominent peaks of COV_{A_s} (Figure 21b). The fast advancement of the
764 wetting front suggests that, in these cases, the peaks might have occurred between 0.5 and
765 5 days, hence they are not shown in Figure 21b. Conversely, the COV_{A_s} for $m = 0.2$
766 exhibits a sharp peak indicating a large spread of failure mechanisms at 5 days and hence
767 a large variation of A_s between realisations as previously discussed. As before, the slower

768 advancement of the wetting front delays the attainment of the peak value of COV_{A_s} to 10
 769 days for the two cases of $m = 0.4$ and 0.8 (Figure 21b).

770

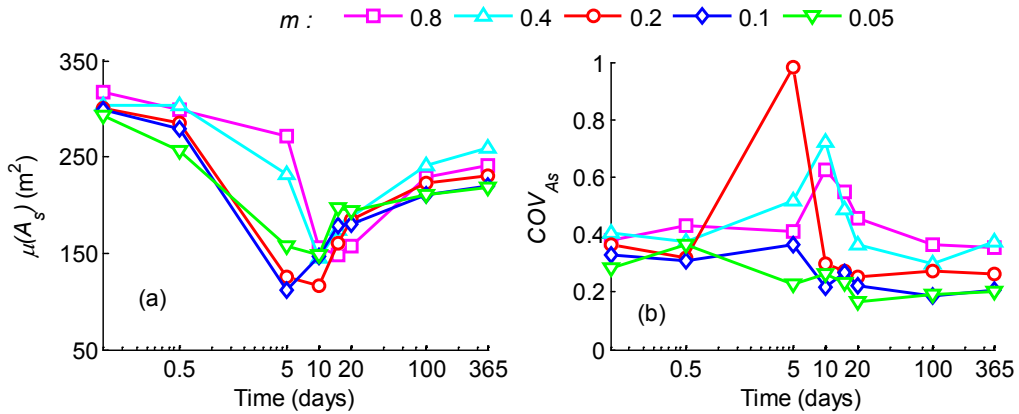


771

772 Figure 20: Time evolution of FoS in terms of mean (a) and coefficient of variation (b).

773 Analyses: influence of the SWRC (parameter m).

774



775

776 Figure 21: Time evolution of A_s in terms of mean (a) and coefficient of variation (b).

777 Analyses: influence of the SWRC (parameter m).

778

779 **5 Conclusions**

780 This study has shown that the interaction between randomly heterogeneous porosity and
781 partial saturation can lead to very complex statistical variations of both factor of safety
782 and failure size in soil slopes exposed to rainfall infiltration. In general, infiltration
783 diminishes the stability of an unsaturated slope but the extent of this effect depends on
784 various factors. If the slope exhibits large porosity variability, results can change
785 significantly among realisations and fluctuate considerably over time, which may lead to
786 different conclusions about the safety of the slope compared to the homogeneous case.
787 Moreover, the statistical variation of the factor of safety and failure size is strongly
788 influenced by other factors such as water table depth, rainfall intensity, saturated
789 permeability and retention parameters.

790

791 The advancement of the wetting front during rainfall has a strong influence on both factor
792 of safety and failure size. If the wetting front attains or surpass a 'critical' depth, failure is
793 confined within the wetted superficial layer with a relatively low factor of safety.
794 Conversely, if the wetting front is shallower than the critical depth, the failure surface
795 penetrates deep in the soil, through both wetted and unwetted regions, with a relatively
796 high factor of safety. During rainfall, the mean values of both factor of safety and failure
797 size decrease because of the progressive reduction of soil suction in the superficial soil
798 layer. These mean values attain their respective minima when the majority of Monte
799 Carlo realisations exhibit wetting fronts deeper than the critical depth. After the end of
800 the rainfall, these mean values increase again as suction is progressively recovered. The
801 coefficients of variation of both factor of safety and failure size also increase until the
802 wetting front attains the critical depth in a significant number of realisations. At this time,
803 the failure mechanism may vary widely from shallow to deep seated, which produces
804 large coefficients of variation.

805

806 An increase in rainfall intensity leads to a faster drop in suction, which elevates the risk
807 of failure. Conversely, a progressive increase of saturated permeability only elevates the
808 risk of failure up to a limit, after which the probability of failure starts to reduce. This is

809 because a very high permeability allows excess pore water pressures to dissipate quickly
810 while a very low permeability impedes infiltration altogether. Both these effects decrease
811 the possibility of failure, which explains why the highest risk corresponds to an
812 intermediate permeability level.

813

814 The effect of porosity on unsaturated permeability is non-monotonic due to the opposite
815 variation of the saturated and relative permeability. This complex behaviour produces
816 rather unexpected patterns of water flow in heterogeneous unsaturated slopes. If the
817 retention curve is independent of porosity, water preferably migrates through high
818 porosity regions but, if a pronounced dependency on porosity is introduced, water tends
819 to move through low porosity areas. Moreover, the risk of failure is significantly higher if
820 a dependency of water retention on porosity is assumed and if the gradient of the
821 retention curve is small to intermediate.

822

823 The progressive infiltration of water reduces both factor of safety and sliding area. This
824 does not mean that a large sliding cannot occur in correspondence of a low factor of
825 safety but only means that a small failure might initially occur triggering a progressively
826 larger mechanism. It also suggests that a more accurate assessment of risk should be
827 based on the likelihood of both slope failure and large sliding area.

828

829 **6 Acknowledgements**

830 The authors would like to acknowledge the support by the centre for research-based
831 innovation Klima2050 - Risk reduction through climate adaptation of buildings and
832 infrastructure to the publication of this paper.

833 **7 References**

834 Alonso, E.E.: Risk analysis of slopes and its application to Canadian sensitive clays.
835 *Géotechnique* **26**(3), 453-472 (1976)

836 Alonso, E.E., Lloret, A.: Evolution in time of the reliability of slope in partially saturated
837 soils. Paper presented at the Fourth International Conference on Application of
838 Statistics and Probability in Soil and Structural Engineering Bologna, Italy,
839 Arnold, P., Hicks, M.A.: Stochastic modelling of unsaturated slope stability. Paper
840 presented at the Fifth International Conference on Unsaturated Soils, Barcelona,
841 Spain,
842 Babu, G.L.S., Mukesh, M.D.: Effect of soil variability on reliability of soil slopes.
843 *Géotechnique* **54**(5), 335-337 (2004)
844 Baecher, G.B., Christian, J.T.: Reliability and statistics in geotechnical engineering.
845 Wiley, Chichester, United Kingdom (2003)
846 Bear, J.: Dynamics of Fluids in Porous Media. Dover, (1972)
847 Bishop, A.W., Alpan, I., Blight, G.E., Donald, I.B.: Factors controlling the strength of
848 partly saturated cohesive soils. Paper presented at the Regional Conference on
849 Shear Strength of Cohesive Soils, Boulder,
850 Cameron, D.A., Jaksa, M.B., Wayne, P., O'Malley, A.: Influence of trees on expansive
851 soils in southern Australia. In: Al-Rawas, A.A., Goosen, M.F.A. (eds.) Expansive
852 soils: recent advances in characterization and treatment. p. 526. Taylor & Francis,
853 London, UK (2006)
854 Cho, S.E.: Probabilistic stability analyses of slopes using the ANN-based response
855 surface. *Computers and Geotechnics* **36**, 787-797 (2009)
856 Cho, S.E.: Probabilistic stability analysis of rainfall-induced landslides considering
857 spatial variability of permeability. *Engineering Geology* **171**, 11-20 (2014).
858 doi:<http://dx.doi.org/10.1016/j.enggeo.2013.12.015>
859 Cho, S.E., Lee, S.R.: Instability of unsaturated soil slopes due to infiltration. *Computers*
860 *and Geotechnics* **28**(3), 185-208 (2001)
861 Dou, H.-q., Han, T.-c., Gong, X.-n., Zhang, J.: Probabilistic slope stability analysis
862 considering the variability of hydraulic conductivity under rainfall infiltration–
863 redistribution conditions. *Engineering Geology* **183**, 1-13 (2014).
864 doi:<http://dx.doi.org/10.1016/j.enggeo.2014.09.005>
865 El-Ramly, H., Morgenstern, N.R., Cruden, D.M.: Probabilistic assessment of stability of a
866 cut slope in residual soil. *Géotechnique* **55**(1), 77-84 (2005)
867 Escario, V., Saez, J.: The shear strength of partly saturated soils. *Géotechnique* **36**(3),
868 453-456 (1986)
869 Fenton, G.A.: Simulation and analysis of random field. Ph.D, Princeton University (1990)
870 Fenton, G.A., Griffiths, D.V.: A slope stability reliability model. In, London, Ontario
871 2005. Proceeding of the K.Y.Lo Symposium
872 Fredlund, D.G., Morgenstern, N.R., Widger, R.A.: The shear strength of an unsaturated
873 soil. *Canadian Geotechnical Journal* **15**(3), 313-321 (1978)
874 Gan, J.K., Fredlund, D.G., Rahardjo, H.: Determination of the shear strength parameters
875 of an unsaturated soil using the direct shear test. *Canadian Geotechnical Journal*
876 **25**(3), 500-510 (1988)
877 Griffiths, D.V., Fenton, G.A.: Probabilistic Slope Stability Analysis by Finite Elements.
878 *Journal of Geotechnical and Geoenvironmental Engineering* **130**(5), 507-518
879 (2004)
880 Griffiths, D.V., Huang, J., Fenton, G.A.: Probabilistic Slope Stability Analysis using
881 RFEM with Non-Stationary Random Fields. In: Schweckendiek, T.T., Tol,

882 A.F.F.v., Pereboom, D.D., Staveren, M.T.M.v., Cools, P.M.C.B.M.P. (eds.)
883 Geotechnical Safety and Risk V Rotterdam, Netherlands 2015, pp. 704 - 709

884 Griffiths, D.V., Marquez, R.M.: Three-dimensional slope stability analysis by elasto-
885 plastic finite elements. *Geotechnique* **57** (2007)

886 Hicks, M.A.: Risk and variability in geotechnical engineering. *Géotechnique* **1**(55), 1-2
887 (2005)

888 Hicks, M.A., Chen, J., Spencer, W.A.: Influence of spatial variability on 3D slope
889 failures. In: Brebbia, C.A., Beriatos, E. (eds.) Proceedings of 6th International
890 Conference on Computer Simulation in Risk Analysis and Hazard Mitigation,
891 Thessaly, Greece 2008, pp. 335-342

892 Hicks, M.A., Onisiphorou, C.: Stochastic evaluation of static liquefaction in a
893 predominantly dilative sand fill. *Géotechnique* **55**(2), 123–133 (2005)

894 Hicks, M.A., Samy, K.: Influence of heterogeneity on undrained clay slope stability.
895 *Quarterly J. Engineering Geology and Hydrogeology* **35**(1), 41–49 (2002)

896 Hicks, M.A., Spencer, W.A.: Influence of heterogeneity on the reliability and failure of a
897 long 3D slope. *Comput Geotech* (2010). doi:doi:10.1016/j.compgeo.2010.08.001

898 Kozeny, J.: Über kapillare Leitung des Wassers im Boden. *Akad. Wiss. Wien* **136**(2a),
899 271-306 (1927)

900 Lacasse, S., Nadim, F.: Uncertainties in characterizing soil properties. In: C. D.
901 Shackelford, Nelson, P.P. (eds.) *Uncertainty in the geologic environment*. pp. 49-
902 75. ASCE, New York (1996)

903 Le, T.M.H.: *Stochastic Modelling of Slopes and Foundations on Heterogeneous*
904 *Unsaturated Soils*. The University of Glasgow (2011)

905 Le, T.M.H., Eiksund, G., Strøm, P.J.: Statistical characterisation of soil porosity. In:
906 Deodatis, G., Ellingwood, B., Frangopol, D. (eds.) *Proceeding of the 11th In*
907 *International Conference on Structural Safety & Reliability*, Columbia University,
908 New York, USA, June 16 - 20, 2013 2013. CRC Press/Balkema

909 Le, T.M.H., Gallipoli, D., Sánchez, M., Wheeler, S.: Stability and failure mass of
910 unsaturated heterogeneous slopes. *Canadian Geotechnical Journal* **52**(11), 1747-
911 1761 (2015). doi:10.1139/cgj-2014-0190

912 Le, T.M.H., Gallipoli, D., Sanchez, M., Wheeler, S.J.: Stochastic analysis of unsaturated
913 seepage through randomly heterogeneous earth embankments. *International*
914 *Journal for Numerical and Analytical Methods in Geomechanics* **36**(8), 1056-
915 1076 (2012). doi:10.1002/nag.1047

916 Mostyn, G.R., Li, K.S.: Probabilistic slope analysis: state-of-play. In, Canberra, Australia
917 1993. *Proceedings of the conference on probabilistic methods in geotechnical*
918 *engineering*, pp. 89-109

919 Mostyn, G.R., Soo, S.: The effect of autocorrelation on the probability of failure of
920 slopes. In: *Proceedings of 6th Australia, New Zealand Conference on*
921 *Geomechanics: Geotechnical Risk 1992*, pp. 542-546

922 Olivella, S., Gens, A., Carrera, J., Alonso, E.: Numerical formulation for a simulator
923 (CODE-BRIGHT) for the coupled analysis of saline media. *Engineering*
924 *Computations* **13**(7), 87-112 (1996)

925 Pathak, D.R., Gharti, H.N., Singh, A.B., Hiratsuka, A.: Stochastic modeling of
926 progressive failure in heterogeneous soil slope. *Geotech Geol Eng* (2007)

927 Phoon, K.-K., Santoso, A., Quek, S.-T.: Probabilistic Analysis of Soil-Water
928 Characteristic Curves. *Journal of Geotechnical and Geoenvironmental*
929 *Engineering* **136**(3), 445-455 (2010). doi:doi:10.1061/(ASCE)GT.1943-
930 5606.0000222

931 Rodríguez, R., Sánchez, M., Lloret, A., Ledesma, A.: Experimental and numerical
932 analysis of a mining waste desiccation. *Canadian Geotechnical Journal* **44**, 644-
933 658 (2007)

934 Santoso, A.M., Phoon, K.-K., Quek, S.-T.: Effects of soil spatial variability on rainfall-
935 induced landslides. *Computers and Structures* **89**(11-12), 893-900 (2011).
936 doi:10.1016/j.compstruc.2011.02.016

937 Sejnoha, M., Sejnoha, J., Kalousková, M., Zeman, J.: Stochastic analysis of failure of
938 earth structures. *Probabilistic Engineering Mechanics* **22**(2), 206-218 (2007)

939 Tsaparas, I., Rahardjo, H., Toll, D.G., Leong, E.C.: Controlling parameters for rainfall-
940 induced landslides. *Computers and Geotechnics* **29**(1), 1-27 (2002)

941 UPC: CODE_BRIGHT User's Guide: A 3-D program for thermo-hydro-mechanical
942 analysis in geological media. Cent. Int. de Metodos Numericos en Ing. Univ.
943 Politecnica de Catalunya, Department of Geotechnical Engineering and
944 Geosciences, Barcelona, Spain (2010)

945 van Genuchten, M.T.: A closed form equation for predicting the hydraulic conductivity of
946 unsaturated soils. *Soil Science Society of America Journal* **44**, 892-898 (1980)

947 van Genuchten, M.T., Nielsen, D.R.: On describing and predicting the hydraulic
948 properties of unsaturated soils. *Annales Geophysicae* **3**(5), 615-627 (1985)

949 Xia, Y., Mahmoodian, M., Li, C.-Q., Zhou, A.: Stochastic Method for Predicting Risk of
950 Slope Failure Subjected to Unsaturated Infiltration Flow. *International Journal of*
951 *Geomechanics* **17**(8) (2017)

952 Zandarín, M.T., Oldecop, L.A., Rodríguez, R., Zabala, F.: The role of capillary water in
953 the stability of tailing dams. *Engineering Geology* **105**, 108-118 (2009)

954 Zhang, J., Huang, H.W., Zhang, L.M., Zhu, H.H., Shi, B.: Probabilistic prediction of
955 rainfall-induced slope failure using a mechanics-based model. *Engineering*
956 *Geology* **168**, 129-140 (2014). doi:<http://dx.doi.org/10.1016/j.enggeo.2013.11.005>

957 Zhang, L.L., Zhang, L.M., Tang, W.H.: Technical note: Rainfall-induced slope failure
958 considering variability of soil properties. *Géotechnique* **55**(2), 183-188 (2005)

959 Zhu, T.: Some Useful Numbers on the Engineering Properties of Materials -GEOL 615
960 Course note
961 <http://www.stanford.edu/~tyzhu/Documents/Some%20Useful%20Numbers.pdf>
962 (2014). Accessed 23 May 2014
963